

Fast Coherent Control of a Nitrogen-Vacancy-Center Spin Ensemble Using a KTaO_3 Dielectric Resonator at Cryogenic Temperatures

Hyma H. Vallabhapurapu^{1,*}, James P. Slack-Smith,² Vikas K. Sewani,¹ Chris Adambukulam,² Andrea Morello,¹ Jarryd J. Pla,² and Arne Laucht^{1,†}

¹Centre for Quantum Computation and Communication Technology, School of Electrical Engineering and Telecommunications, The University of New South Wales, Sydney, New South Wales 2052, Australia

²School of Electrical Engineering and Telecommunications, The University of New South Wales, Sydney, New South Wales 2052, Australia

(Received 19 May 2021; revised 21 August 2021; accepted 1 October 2021; published 26 October 2021)

Microwave delivery to samples in a cryogenic environment can pose experimental challenges such as restricting optical access, space constraints, and heat generation. Moreover, existing solutions that overcome various experimental restrictions do not necessarily provide a large homogeneous oscillating magnetic field over macroscopic length scales, which is required for control of spin ensembles or fast gate operations in scaled-up quantum computing implementations. Here, we show fast and coherent control of a negatively charged nitrogen-vacancy spin ensemble by taking advantage of the high permittivity of a KTaO_3 dielectric resonator at cryogenic temperatures. We achieve Rabi frequencies of up to 48 MHz, with a total power-to-field conversion factor $C_P = 9.66 \text{ mT}/\sqrt{\text{W}}$ (approximately $191 \text{ MHz}_{\text{Rabi}}/\sqrt{\text{W}}$). We use the nitrogen-vacancy-center spin ensemble to probe the quality factor, the coherent enhancement, and the spatial distribution of the magnetic field inside the diamond sample. The key advantages of the dielectric resonator utilized in this work are ease of assembly, *in situ* tunability, a high magnetic field conversion efficiency, a low-volume footprint, and optical transparency. This makes KTaO_3 dielectric resonators a promising platform for the delivery of microwave fields for the control of spins in various materials at cryogenic temperatures.

DOI: 10.1103/PhysRevApplied.16.044051

I. INTRODUCTION

Fast spin control—much faster than the coherence time—is essential for achieving truthful and high-fidelity qubit gate operations [1,2]. While dynamical decoupling and error correction can be used to somewhat mitigate decoherence effects, they only work once a certain fidelity threshold has already been met [3,4]. In the context of spin qubit control, microwave (MW) resonators can allow for an efficient interaction with the spin qubits of interest [5–8]. In particular, the enhancement of the oscillating magnetic field (B_1) offered by such a resonator can result in high-frequency Rabi oscillations of the spins, and thus fast gate operations, while keeping the input power at a moderate level. A prominent figure of merit is the B_1

power-to-field conversion factor C_P , which can be accurately estimated by measuring the Rabi frequency Ω_R of the spins through the relationship $\Omega_R = (1/\sqrt{2})\gamma_e B_1 = (1/\sqrt{2})\gamma_e C_P \sqrt{P_{\text{MW}}}$ (for $m_s = 1$), where $C_P = B_1/\sqrt{P_{\text{MW}}}$ and γ_e is the electron gyromagnetic ratio.

For cryogenic environments, a suitable MW field delivery method designed for optically active spin defects is yet to be realized, especially one that is homogeneous enough for ensemble measurements. Some favorable attributes of an ideal MW delivery apparatus for such an application include optical transparency, a high B_1 conversion factor at cryogenic temperatures, *in situ* resonance-frequency tunability, and simple design and implementation. Existing solutions include conventional antenna and resonator designs [9–17] and spin-wave-mediated methods [18], but lack in one or more of the aforementioned characteristics.

Critically, high-speed quantum gate operations require fast Rabi oscillations of the spin qubit, ultimately benefiting from a high C_P . Typically, such high C_P can be achieved using nanoscale lithographically defined on-chip antennas [19] and superconducting resonators [20]. However, these structures require complex on-chip fabrication and their use is often restricted to spins located in

*h.vallabhapurapu@unsw.edu.au

†a.laucht@unsw.edu.au

Published by the American Physical Society under the terms of the [Creative Commons Attribution 4.0 International license](#). Further distribution of this work must maintain attribution to the author(s) and the published article's title, journal citation, and DOI.

close proximity to the antenna structure. Despite benefiting from a high C_P , practically achievable Rabi frequencies range from 100 kHz to 3 MHz due to various damage thresholds and superconductivity limitations including critical current limits. However, Rabi oscillations as fast as 440 MHz have also been achieved outside a cryostat [21] using similar structures. The highest reported C_P for macroscopic MW resonators in the literature are $1.19 \text{ mT}/\sqrt{\text{W}}$ ($23.60 \text{ MHz}_{\text{Rabi}}/\sqrt{\text{W}}$) [10,16] for planar split-ring resonators, $1.17 \text{ mT}/\sqrt{\text{W}}$ ($23.16 \text{ MHz}_{\text{Rabi}}/\sqrt{\text{W}}$) for a rutile dielectric loop-gap resonator [15], and $3.2 \text{ mT}/\sqrt{\text{W}}$ ($89.60 \text{ MHz}_{\text{Rabi}}/\sqrt{\text{W}}$) for a microhelix resonator [22].

Dielectric resonators in particular have played a prominent role in spin-resonance experiments [23] with regard to enhancement of the MW excitation field [24,25] and demonstration of the spin-cavity coupling dynamics [7, 8,26–28]. KTaO_3 is a quantum paraelectric material possessing low MW losses ($\tan \delta \sim 10^{-4} - 10^{-5}$) and high permittivity ($\epsilon_r \approx 4300$ for $T < 10 \text{ K}$), making it an encouraging material for delivering high MW fields at cryogenic temperatures [29], in contrast to commonly used dielectrics such as rutile and sapphire [30,31], which possess ϵ_r up to 2 orders of magnitude lower. For a given frequency, the required dimensions of the dielectric resonator scales as a function of $\sqrt{\epsilon_r}$ [24]. A significant reduction in size is expected of KTaO_3 resonators compared to sapphire or rutile resonators at cryogenic temperatures. For operation in the gigahertz range, this results in convenient millimeter dimensions for KTaO_3 resonators. Further, due to its good optical properties and high refractive index ($n = 2.3$ for $\lambda = 500 \text{ nm}$ at 300 K), KTaO_3 has been used as a solid immersion lens [32,33], showing great potential for application as a dual-purpose MW resonator that can be used for boosting photon collection efficiency and MW field strength simultaneously for optically detected magnetic resonance of spin defects.

In the past, KTaO_3 dielectric resonators have been used to demonstrate enhanced electron paramagnetic resonance (EPR) sensitivity [25,34,35] (measured $C_P = 1.3 \text{ mT}/\sqrt{\text{W}}$ at 77 K), and for incoherent-spin manipulation of a quantum dot spin qubit in a device based on a Si metal-oxide-semiconductor structure [6]. However, little work has been done to demonstrate coherent control of a solid-state spin—single or ensemble—at cryogenic temperatures.

Here, we demonstrate the use of a KTaO_3 dielectric resonator with internal quality factor $Q_I \approx 1387$ (limited by dissipation in the diamond sample) and $> 100 \text{ MHz}$ *in situ* tunability to deliver high-amplitude oscillating B_1 fields to a $\text{N}-V^-$ spin ensemble in diamond. This allows us to drive fast and coherent Rabi oscillations up to $\Omega_R = 48 \text{ MHz}$ and, conversely, use the $\text{N}-V^-$ spin ensemble to probe the resonator characteristics. We measure a conversion factor C_P of $9.66 \text{ mT}/\sqrt{\text{W}}$ (approximately $191 \text{ MHz}_{\text{Rabi}}/\sqrt{\text{W}}$) and an approximately 7% spatial B_1 inhomogeneity over

the 0.4 mm central region. By performing T_2^{Rabi} and T_2^{Hahn} echo measurements, we identify the dominant limitation to the control fidelity to be the B_1 inhomogeneity within the signal collection volume and a slight misalignment of the B_1 field with respect to the crystallographic axis of the diamond sample.

We choose an ensemble of negatively charged nitrogen-vacancy ($\text{N}-V^-$) centers in diamond [36] to characterize the dielectric resonator due to the high spin-dependent photoluminescence contrast down to cryogenic temperatures. $\text{N}-V^-$ centers in diamond have a wide range of applications in the field of magnetometry [37]. The spin ensemble conveniently allows us to spatially map the B_1 field of the dielectric resonator within the diamond; similar mapping of the B_1 field of other resonators has been demonstrated in the literature [11,16,38–40]. Finally, color centers in diamond provide a promising qubit platform for practical implementations of future quantum networks and computers [41–44]—thus it is useful to develop such methods to demonstrate compatibility with diamond-based spins.

II. RESULTS

A. Experimental setup and methods

1. Setup and samples

Our measurement setup is illustrated in Fig. 1(a). It consists of MW circuitry to measure the input-port reflection parameter (S_{11}) of the coaxial loop coupler using a vector network analyzer (VNA). This circuitry allows the resonator to be driven by a MW source while simultaneously monitoring the resonance during measurements. The optical part of the setup is used to optically interact with the $\text{N}-V^-$ spin ensemble. The optical setup delivers a 520-nm green laser for off-resonant excitation of the $\text{N}-V^-$ centers with a focused-beam spot diameter of approximately $5 \mu\text{m}$ (see Table V). The resulting emission from the $\text{N}-V^-$ is then collected by the same optical setup via a different optical path using an appropriate dichroic mirror. The optical setup also delivers an 785-nm infrared laser for *in situ* thermal tuning and stabilization of the dielectric resonator (see Fig. 7). A lens with a long focal length of 15.29 mm is used to focus all the lasers into the diamond sample, while also collecting the $\text{N}-V^-$ photoluminescence.

A $2.6 \times 2.6 \times 0.25 \text{ mm}^3$ diamond sample containing an $\text{N}-V^-$ spin density of approximately $6 \times 10^{11} \text{ spins/mm}^3$ (grown by chemical vapor deposition with $\langle 100 \rangle$ orientation) is sandwiched between two KTaO_3 prisms ($1.8 \times 1.8 \times 0.5 \text{ mm}^3$) that form the dielectric resonator (see Fig. 5(a) in the Appendix). The samples are placed on a piezoelectric sample stage (Attocube), which allows repositioning of the samples inside the cryostat. Finally, a loop coupler positioned above the samples is used to couple to the dielectric resonator inside the cryostat such that the resonator is operating in the overcoupled regime [see

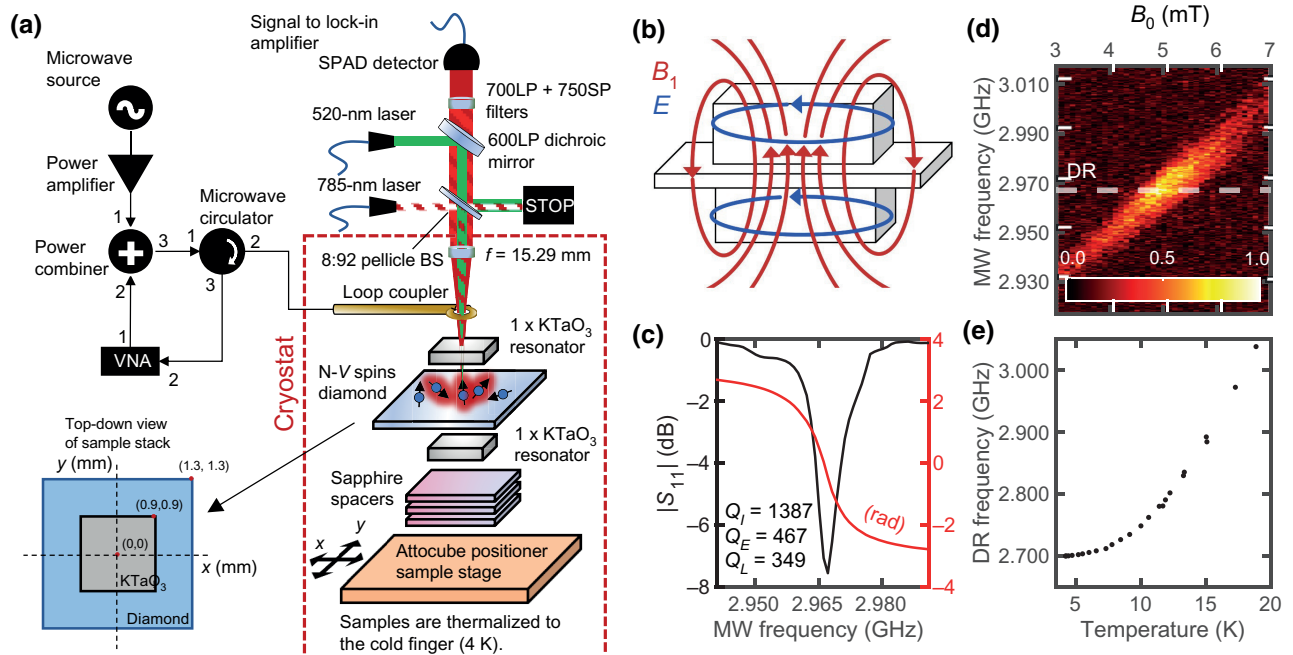


FIG. 1. The setup and the ODMR response. (a) An overview of the measurement setup, showing the schematic of the microwave circuit, an exploded view of the optical setup, and the sample mounting. The samples are mounted on an Attocube piezoelectric stage, allowing the samples to be repositioned inside the cryostat. (b) A sketch of the magnetic (red) and electric (blue) field lines corresponding to the $\text{TE}_{11\delta}$ excitation mode of the dielectric resonator. (c) The reflection magnitude and phase signals of the overcoupled KTaO_3 dielectric resonator, when tuned through a fixed microwave reference frequency at 2.967 GHz. (d) The ODMR signal as a function of the microwave frequency and the magnetic field B_0 . The white dashed line indicates the dielectric resonator frequency. (e) The measured temperature dependence of the dielectric resonator (DR) frequency in the cryostat.

Figs. 5(b) and 6]. The coupling of the loop coupler to the dielectric resonator is shown in Fig. 1(c), with loaded and internal quality-factor fits of $Q_L = 349 \pm 5$ and $Q_I = 1388 \pm 6$, respectively. The fundamental $\text{TE}_{11\delta}$ -like mode of the KTaO_3 dielectric resonator is used for all measurements, illustrated in Fig. 1(b). The single-spin-to-cavity coupling strength is $g_s/2\pi \approx 1$ Hz, approximately given by $\gamma_e \sqrt{\mu_0 \hbar w_0 / (2V_m)}$ [28] for a simulated mode volume $V_m = 0.98 \text{ mm}^3$ (see Sec. 2 of the Appendix). The parameters μ_0 , \hbar , and w_0 are the permeability of free space, the reduced Planck's constant, and the resonator frequency, in units of radians per second, respectively.

2. Optically detected magnetic resonance measurements

All spin experiments are performed using pulsed optically detected magnetic resonance (ODMR) to observe the absolute change in photoluminescence as a result of transferring the spin population from the $|0\rangle$ initial state to the $|+\rangle$ state [45,46], using a lock-in amplifier. A superconducting magnet is used to sweep the static B_0 field; it is set to persistence mode when the B_0 field is required to be fixed in order to ensure B_0 stability. All error bars for measurement fits are given as 95% confidence intervals.

3. Resonator tuning

The permittivity of the KTaO_3 material varies as a function of the temperature [29]. This allows the resonator to be continuously tuned to 2.967 GHz or another predetermined frequency via heating using the 785-nm laser (see Fig. 7), corresponding to a local resonator temperature of 17 K, estimated using the measured frequency versus cryostat temperature curve shown in Fig. 1(e). The temporal stability of the resonance frequency is recorded throughout the measurements and is shown in Fig. 11. Apart from the thermal tuning technique, the dielectric resonator is further stabilized by employing pulse compensation wherein the total duty cycle of the laser and MW pulses are kept constant in the ODMR pulse sequences (see Fig. 8).

Additional details of the experimental setup can be found in Sec. 1 of the Appendix.

B. ODMR-signal enhancement

We start by performing incoherent ODMR measurements using the measurement setup shown in Fig. 1(a), to observe the ODMR-signal enhancement. In Fig. 1(d), we sweep B_0 to tune the N-V⁻ spin transitions through the MW dielectric resonance. The measurement is performed using low MW power (-11 dBm) at the loop coupler and long MW pulses ($40 \mu\text{s}$) to reduce power broadening and

to ensure that the spins are incoherently driven. The result clearly shows the increase in the spin-dependent fluorescence signal when the $N-V^-$ frequency is in the vicinity of the cavity resonance. Integration of the ODMR signal for the on-resonance and off-resonance cases presents an ODMR-signal enhancement factor of 1.7.

C. B_1 field conversion

Next, we extract the power-to-field conversion factor C_P by measuring the Rabi frequency Ω_R of the spin ensemble as a function of the applied MW power P_{MW} over 3 orders of magnitude. The measurements are performed with the MW source, $N-V^-$, and resonator frequencies in resonance at 2.967 GHz, as shown in Fig. 1(c), corresponding to $B_0 = 5$ mT. We plot the Rabi oscillations for selected MW powers in Fig. 2(a). We fit the oscillations to decaying sinusoids (red lines) and plot the extracted Rabi frequencies (Ω_R) and Rabi decay rates ($1/T_2^{\text{Rabi}}$) in Fig. 2(b). The Ω_R data (filled circles) in Fig. 2(a) is then fitted to a linear function of \sqrt{W} with a gradient of $C_P = 156 \pm 2$ MHz $_{\text{Rabi}}/\sqrt{W}$, representing the measured Rabi-frequency conversion factor. After compensating for the oscillating field within the rotating-wave approximation and the misalignment between the B_1 direction and

the $N-V^-$ quantization axis (see Sec. 4 of the Appendix), we find the total B_1 conversion factor to be 9.66 mT/ \sqrt{W} , corresponding to a theoretical Rabi-frequency conversion factor of 191 MHz $_{\text{Rabi}}/\sqrt{W}$. This conversion factor is in good agreement with the simulated results (see Sec. 2 of the Appendix), as shown in Fig. 9(c), as well as the theoretically predicted mean value [47]

$$\langle C_P \rangle = \mu_0 \sqrt{\frac{2Q_L}{\mu_0 V_m \omega_0}} \approx (7\text{mT}/\sqrt{W}). \quad (1)$$

The C_P measured in this work is at least a factor of 7 larger than those reported for dielectric resonators in the literature [15,35], including previously reported KTaO₃ resonators, and at least a factor of 3 larger than other resonators [10,16,22]. This is a considerable improvement, as to achieve the same B_1 fields shown in this work using other resonators would typically require at least a +9 dB addition of MW power, which can be difficult to achieve in millikelvin cryostats.

B_1 conversion factors up to an order of magnitude higher should be achievable with higher quality factors of the dielectric resonator, as can be predicted from Eq. (1)—for example, by using an electronic grade diamond sample that exhibits lower loss (see Table III in the Appendix). High

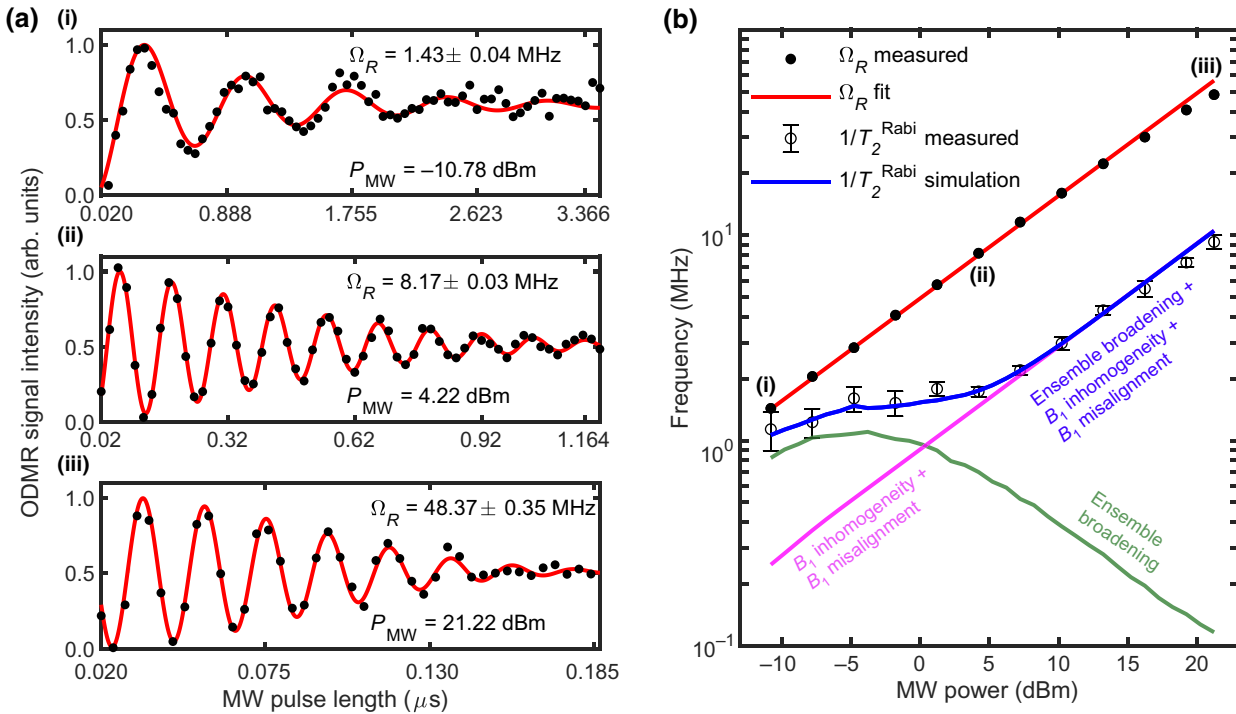


FIG. 2. The B_1 conversion factor and the Rabi decay rate. (a) Selected Rabi oscillation measurements at three microwave powers, specified at the loop coupler. The red lines are fits to the measured data with a decaying sinusoidal function including an exponent n . (b) The measured Rabi frequency is shown to double for +6-dB increments of microwave power, as expected (the red fit excludes the last three data points due to amplifier saturation). The trend of the $1/T_2^{\text{Rabi}}$ decay rate (blue line) can be explained by power broadening. This leads, in combination with the spectral distribution of the ensemble (green line) and the B_1 inhomogeneity within the detection volume (magenta line), to the observed S bend.

quality factors are expected to proportionally increase the ringdown time of the resonator. It is trivial to see that the final spin state is directly dependent on the integral of the applied MW pulse signal. Therefore, a short square-shaped MW pulse is approximately equivalent to a resulting bandwidth-limited MW pulse, given that the spins are not reinitialized before the ringdown time $\tau = 2(Q_L/\omega_0)$. This is appropriately accounted for in the measurements by using a delay time (of the order of 100 ns) between the microwave pulse and a subsequent laser readout pulse within a relevant pulse sequence. However, this may not be necessary for applications utilizing a “global” MW field [6], wherein the spin system can instead be arbitrarily brought into and out of resonance of the MW field for coherent control. Alternatively, shaped MW pulses may be used to achieve ringdown suppression [48].

The open circles in Fig. 2(b) depict the corresponding Rabi decay rate $1/T_2^{\text{Rabi}}$. The observed S-bend trend can be explained as follows. At low MW powers, the dominant limitation to T_2^{Rabi} is the ensemble broadening given by the hyperfine coupling to the ^{14}N nuclear spins and the four $\text{N}-\text{V}^-$ center axes that form slightly different angles with respect to B_0 , leading to the summation of signals from 12 transitions at varying detuning from the excitation frequency. When increasing P_{MW} , power broadening improves T_2^{Rabi} [44] when it becomes greater than the inhomogeneous spin-ensemble line width, leading to an inflection in the decay rate trend. At even higher P_{MW} , we find that T_2^{Rabi} is limited by the B_1 inhomogeneity, leading to an increase in $1/T_2^{\text{Rabi}}$ that is directly proportional to Ω_R . This B_1 inhomogeneity manifests as a combination of the spatial variation of the B_1 field produced by the dielectric resonator within the signal collection volume (limited by the laser focus), and the different effective B_1 strengths corresponding to the four unique $\text{N}-\text{V}^-$ orientations within the diamond crystal lattice due to some misalignment with respect to their quantization axes [46].

We perform numerical simulations considering the aforementioned effects, with results shown in Fig. 2(b). The simulated Rabi decay rates (blue line) are in good agreement with the experimental data (open circles). In the same figure, we also show the individual contributions of the B_1 inhomogeneity (magenta line) and ensemble broadening (green line) toward the total Rabi decay rate. More information about the simulation model can be found in Sec. 5 of the Appendix. A collection of measured and simulated Rabi oscillations can be seen in Fig. 12.

D. Coherent B_1 enhancement

In this section, we investigate the detuning dependence of the B_1 field enhancement by the dielectric resonator, by measuring the Rabi frequencies for various resonator-frequency detunings relative to the $\text{N}-\text{V}^-$ and MW source frequency. We therefore fix the MW source to 2.967 GHz

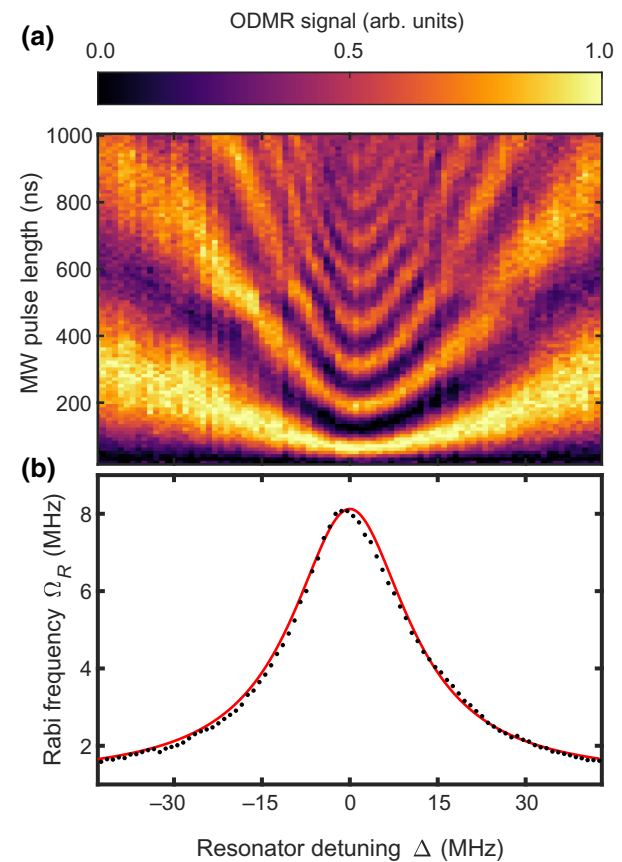


FIG. 3. The detuning dependence of the Rabi oscillation enhancement. (a) The chevron pattern of the Rabi oscillations plotted against a range of $\text{N}-\text{V}^-$ -resonator detunings. The microwave source is kept in resonance with the $\text{N}-\text{V}^-$ ODMR frequency throughout this measurement. (b) The corresponding Rabi frequencies fitted to a Lorentzian function. The on-resonance enhancement is calculated as approximately $7.1 \times$.

and the B_0 field to approximately 5 mT, such that the $\text{N}-\text{V}^-$ transitions are in resonance with the driving field and sweep the resonator frequency through various pre-determined detuning frequencies using the 785-nm laser. This method ensures that frequency-dependent interference in the cables does not lead to a variation in the MW power arriving at the dielectric resonator. The measurement results in a chevronlike pattern of Rabi oscillations, which we plot in Fig. 3(a). We extract the resulting Rabi oscillation frequencies Ω_R and plot them as a function of the resonator detuning Δ in Fig. 3(b). The red line is a Lorentzian fit to the data.

The line-width fit of Ω_R^2 is found to be 15.6 MHz and corresponds to the full-width-at-half-maximum line width for a 3 dB drop in microwave power. This line width is a result of the convolved line widths of the resonator and that of the ensemble-broadened spin resonance. The spin-resonance line width can be approximated as 7.1 ± 1.7 MHz using the average ODMR line width of the detuned

ODMR resonance ($B_0 \approx 3$ mT) from Fig. 1(d). The bare-resonator line width is thus simply calculated as the difference 8.5 ± 1.7 MHz, corresponding to a $Q_L = 351^{+86}_{-58}$. This is in good agreement with the resonator line width and quality factor measured by the VNA, shown in Fig. 1(c).

On resonance, we observe a coherent enhancement factor of 7.1 for the ODMR signal, higher than the incoherent enhancement shown in Fig. 1(d). This is due to the fact that Ω_R provides an accurate direct measurement of B_1 , while the enhancement of the incoherent ODMR signal is an indirect measurement of a spin ensemble in a mixed state and subject to saturation effects.

In addition to the detuning dependence of the B_1 enhancement, the measurement in Fig. 3 also demonstrates the resonance-frequency tunability of the dielectric resonator via heating with the 785-nm infrared laser (for more details on resonator-frequency tuning and stabilization, see also Sec. 1 of the Appendix). In this measurement, we tune the resonator over a range of approximately 90 MHz. Such tunability allows for some flexibility in the dielectric resonator dimensions and is useful in experiments where the B_0 field cannot be adjusted [49] or where ODMR transitions may be selectively enhanced without needing to adjust the B_0 field.

E. Spatial B_1 field distribution and coherence

We map the B_1 distribution along the x and y axes by measuring the corresponding Rabi oscillation frequencies Ω_R and their decay times T_2^{Rabi} at various positions across the sample for a fixed MW excitation power. Since the sample is repositioned (using the Attocube piezoelectric positioner) to obtain this measurement, the coupling between the loop coupler and the dielectric resonator is expected to change. We numerically compensate the measured Rabi frequencies by accounting for the reflection magnitude (S_{11}) as measured by the VNA (more details are given in Sec. 5 of the Appendix). We plot the compensated Ω_R and Rabi decay rates $1/T_2^{\text{Rabi}}$ along the x and y axes in Figs. 4(a) and 4(b), respectively. Ω_R varies between 8 MHz at the center and about 5 MHz when the sample is moved 0.5 mm in either direction. Quite remarkably, over the 0.4-mm center region (i.e., $-0.2 \text{ mm} < x, y < +0.2 \text{ mm}$), Ω_R only decreases by approximately 7%. The $1/T_2^{\text{Rabi}}$ decay rates are found to be generally lower toward the center of the resonator, due to the better B_1 homogeneity in the x - y plane.

To obtain further proof that T_2^{Rabi} is limited by the increase in B_1 inhomogeneity toward the edges of the sample, we perform Hahn-echo measurements at different positions along the x axis (see Fig. 13). In a Hahn-echo sequence, constant- B_0 inhomogeneities are refocused and only noise with frequencies at the measurement time scale matters. Furthermore, variations in the B_1 amplitude only affect the measurement contrast and not the T_2^{Hahn} decay

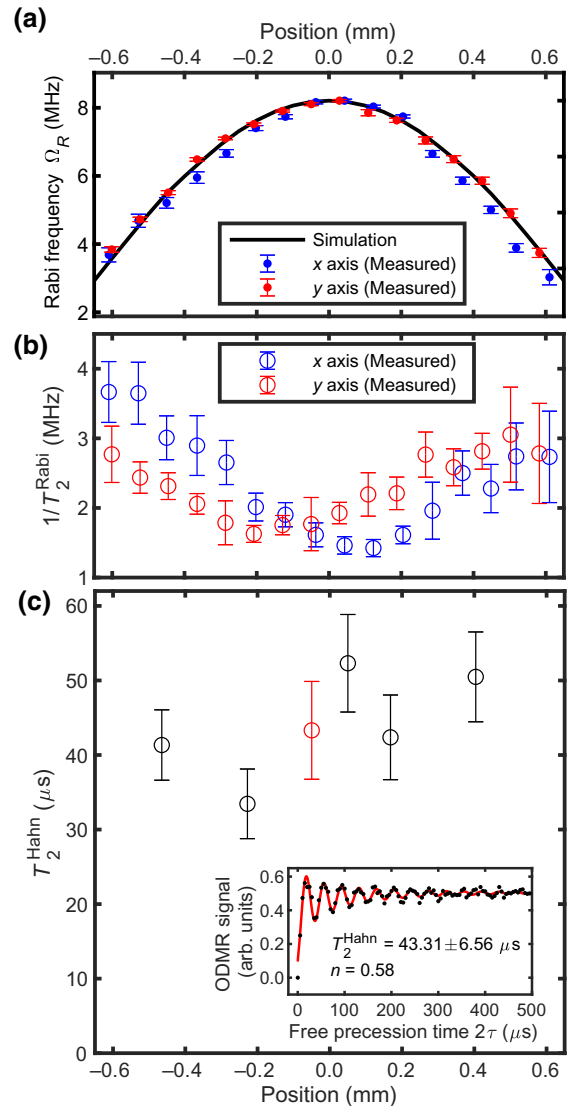


FIG. 4. The position dependence and homogeneity of B_1 enhancement. (a) The measured and appropriately compensated Rabi frequency Ω_R along the x and y axes of the diamond sample [see Eq. (A1) in the Appendix]. The black line corresponds to predicted Ω_R values, obtained from modeling the trend of the B_1 field of the dielectric resonator in CST MICROWAVE STUDIO. We find good agreement between the experimental data and the CST simulation model. (b) $1/T_2^{\text{Rabi}}$ decay rates measured and plotted across both axes of the sample. We observe a general increase in T_2^{Rabi} coherence times toward the center of the resonator, due to higher B_1 homogeneity. (c) T_2^{Hahn} decay times for positions along the x axis of the resonator. We do not observe significant variations of the T_2^{Hahn} decay times across the sample. The inset shows a sample Hahn-echo measurement for a position close to the center of the resonator, corresponding to the data point highlighted in red in the main panel. The error bars represent 95% confidence intervals for fits.

time. The data are fitted to the appropriate exponential decay function [50], including the exponent n as an additional fit parameter. The extracted T_2^{Hahn} decay times are all

around $35 - 55 \mu\text{s}$ [see Fig. 4(c)], in accordance with the literature values for our sample type, temperature, and B_0 misalignment, and thus likely limited by noise processes within the diamond sample [51–53]. Overall, the results show no significant variation across the sample, suggesting little variation of dynamic noise across the dielectric resonator and confirming our assumption that T_2^{Rabi} is limited by the inhomogeneity in B_1 .

III. CONCLUSION

We demonstrate fast coherent control and ODMR measurements of an N-V^- center ensemble, utilizing the appreciable conversion factor C_p provided by the KTaO_3 dielectric resonator. The simple assembly of the dielectric resonator with the diamond sample, its *in situ* tunability, its low-volume footprint, its and optical transparency are presented as key advantages in this work.

We measure Rabi frequencies of up to 48 MHz and a total B_1 field conversion factor of $9.66 \text{ mT}/\sqrt{\text{W}}$ (approximately $191 \text{ MHz}_{\text{Rabi}}/\sqrt{\text{W}}$), which shows at least a factor-of-7 improvement in C_p over similar dielectric resonators in the literature. An even higher B_1 conversion factor should be possible when using a diamond sample with less dissipation, as a consequence of the higher resulting resonator quality factor. We find that the dominant limiting factor for the Rabi coherence time is the inhomogeneity of the B_1 field produced by the resonator within the signal collection volume and the effective B_1 inhomogeneity due to the B_1 field misalignment with the four possible N-V^- axes in the diamond. Both of these effects are completely inconsequential for measurements on single spins.

The large, homogeneous, and long-range distribution of the B_1 fields of the dielectric resonator demonstrated in this work may find useful applications in magnetometry with ensembles of N-V^- defects [37], the “global-control” scheme of spin qubits [6], and may also benefit “indirect-control” nuclear spin techniques [54,55] in suitable hyperfine-coupled spin systems wherein the electron Rabi frequencies are generally required to be higher than the hyperfine strength (in the range of megahertz).

We therefore find KTaO_3 dielectric resonators suitable for MW-enhanced coherent control of optically active spins at cryogenic temperatures, with the exciting prospect of simultaneous application as a solid immersion lens.

ACKNOWLEDGMENTS

We would like to thank Mark Johnson and Irene Fernandez de Fuentes for assistance with the cryogenic measurements in liquid helium. We acknowledge funds from the Australian Research Council via Grant No. CE170100012, and to J.J.P. via Grant No. DE190101397. H.V. and J.P.S.-S. acknowledge support from the Sydney Quantum

Academy. C.A. and A.L. acknowledge support from the University of New South Wales Scientia program.

APPENDIX

1. Samples, apparatus, and methods

A (100)-oriented $2.6 \times 2.6 \times 0.25 \text{ mm}^3$ diamond sample, grown by chemical vapor deposition (Element 6 SC Plate CVD P2 [56]) and containing a dilute N-V^- ensemble, is used to probe the MW field strength and distribution of the resonator. The N-V^- density is estimated based on comparing the photoluminescence intensity under 520-nm excitation against a sample with a known N-V^- density. The resonator structure is arranged out of two $1.8 \times 1.8 \times 0.5 \text{ mm}^3$ KTaO_3 prisms (manufactured by AWI Industries), with the diamond sample sandwiched in between, and is designed to resonate at approximately 2.7 GHz at 4 K. This sandwich arrangement is similar to a split-cylindrical dielectric resonator [57] and helps to create a more homogeneous field distribution along the z axis, as confirmed by simulations [see Figs. 9 and 10(b)]. Three sapphire spacers of 0.5-mm thickness are used to distance the resonators from the conductive surface of the sample stage. The sample stack is held together with a minimal amount of vacuum grease on the sides and is mounted on top of an Attocube sample stage, which allows positioning of the sample stack along the x , y , and z axis. A photo of the sample stack is shown in Fig. 5(a). The sapphire spacers reduce MW losses in the dielectric resonator by physically separating the resonator from the conductive surface of the sample stage. It may be noted that the presence of the sapphire spacers may negatively impact the thermal conduction of heat away from the sample stack diamond and dielectric resonator samples. The optimum thickness of the spacers can be found from a suitable simulation model.

The resonator is excited using a coaxial loop coupler that is positioned approximately 1.5 mm above the resonator stack [see Fig. 5(b)]. The coupling strength to the coaxial loop coupler can be modified by adjusting the sample z position with the Attocube stage. Appropriate coupling to the resonator is ensured by measuring the input-port reflection parameter (S_{11}) of the loop coupler using a vector network analyzer (VNA). At room temperature, we measure the expected reflection dip at 11.2 GHz due to the much lower permittivity ϵ_r at this temperature. Figure 6(a) shows a measurement at critical coupling. At 4 K, the resonance shifts to approximately 2.7 GHz and we demonstrate the various coupling regimes measured with the VNA in Fig. 6(b).

The MW circuit consists of a MW source, an amplifier, a VNA, a power combiner, and a circulator. The circulator is not strictly necessary for our experiments. However, it is used to prevent damage to our MW equipment due to any high-power reflections returning from the cryostat. This is especially important when using a high-gain

and high-power MW amplifier to deliver MW power to a shorted loop coupler. In this way, the circulator directs any reflected MW power through attenuators into port 2 of the VNA. We operate the VNA in S_{21} mode accordingly (this still constitutes a S_{11} reflection measurement on the loop coupler), with a probing power of approximately -40 dBm calculated at the loop coupler. The MW source output is pulse modulated to allow for pulsed spin control. The arrangement of the MW equipment using a power combiner allows for the S_{11} to be measured while performing the coherent-spin control measurements. This allows the resonator to be dynamically tuned during the spin measurements, using the 785-nm laser for heating and the VNA measurement as a feedback input.

Although the KTaO_3 resonance frequency has been shown to be tunable via an application of a suitable electrical field [58], such a tuning mechanism would require conductor traces to be patterned on the resonator structure or the diamond sample. For the sake of simplicity, the dielectric resonator here is tuned thermally by taking advantage of the temperature-sensitive permittivity of KTaO_3 (see Fig. 7). The resonator is tuned to the desired frequency via a simple software-implemented control algorithm with suitably selected proportional and derivative terms through trial and error. This allows the dielectric resonator temperature to be controlled by heating the sample stack with a low-power 785-nm laser. Inspection of Figs. 6(b), 6(i) and 1(c) shows that the loaded quality factor of the dielectric resonator does not significantly change when the frequency of the dielectric resonator is shifted from 2.70 GHz ($Q_L =$

416 corresponding to 4 K) to 2.96 GHz ($Q_L = 349$ corresponding to 17 K). According to Eq. (1), this results in a C_P variation of approximately 12%, which is remarkable considering an effective temperature tuning range of approximately 13 K.

The resonator is tuned continuously in the background during all experiments, since the resonator otherwise exhibits frequency drifts over a short time period, which are attributed to thermal fluctuations caused by the pulsing nature of laser and microwave radiation. Additionally, we also implement a MW pulse sequence wherein we minimize the resonator-frequency drift by ensuring a constant duty cycle (i.e., total pulse time) within each pulse sequence repetition (refer to Fig. 8). We estimate the dielectric resonator temperature to rise by 1.5 K from the base temperature of 4 K with an application of 10 dBm of pulsed microwave power. However, it may be noted that such a large MW power is not required for measurements involving single defects due the lack of ensemble-broadening effects, reducing the thermal load on the cryostat.

The optical setup and measurement principles are adapted from Ref. [46], with an addition of a 785-nm laser and respective optics for resonator tuning. An aspheric lens with a long working distance of 12.43 mm is used to focus the laser beams and collect the sample emission through the topmost dielectric resonator. The use of an aspheric lens with a long working distance results in disadvantages such as chromatic aberration and low NA, which requires higher laser powers to maintain a sufficient

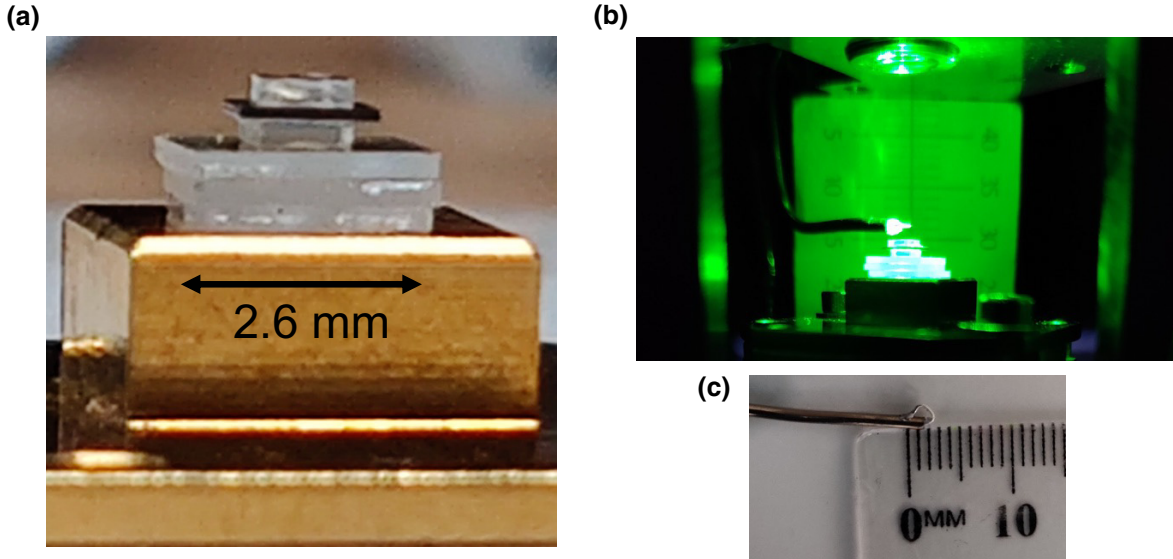


FIG. 5. Setup photographs. (a) The sample stack with the copper stage and the three sapphire spacers below the KTaO_3 dielectric resonator–N-V⁺ diamond sample sandwich. The sample stack is held together with minimal vacuum grease. (b) The sample stack mounted on the dilution refrigerator cold finger atop an Attocube positioner. The coaxial loop coupler is positioned roughly 1.5 mm above the topmost KTaO_3 dielectric resonator. (c) A photograph of the coaxial loop coupler, showing the size of the looped inner conductor.

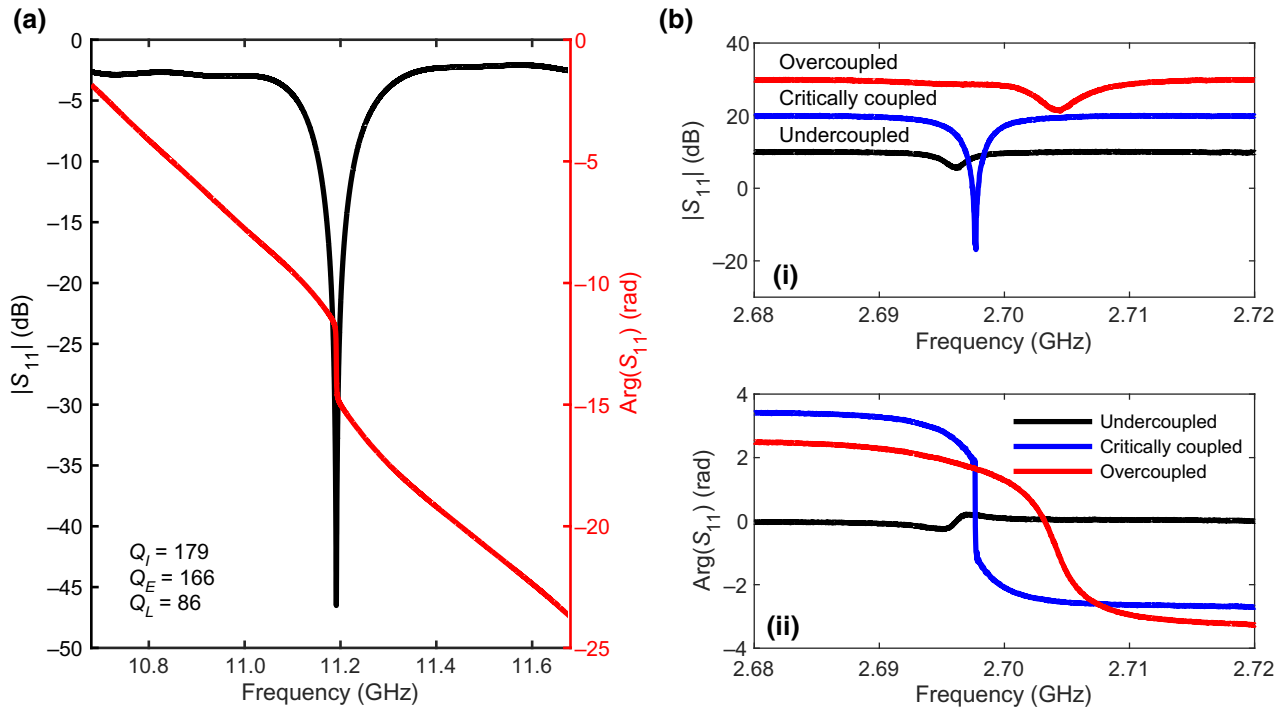


FIG. 6. The loop-coupler–resonator coupling. (a) The VNA measurement of the dielectric resonator stack at room temperature, showing critical coupling. (b) VNA measurements at 4 K showing the S_{11} magnitude (top panel) and phase (bottom panel) for various coupling regimes of the dielectric resonator to the coaxial loop antenna. The coupling strength can be modified by adjusting the sample z position. At critical coupling, $Q_I = 1275 \pm 12$, $Q_E = 1328 \pm 5$, $Q_L = 650 \pm 4$. For the overcoupled case, the values are $Q_I = 1414 \pm 5$, $Q_E = 591 \pm 8$, $Q_L = 416 \pm 7$. The quality factors are extracted using a resonance-fitting script [62]. We attribute the low internal quality factor to the lossy $N-V^-$ CVD diamond sample (see also Table III).

photoluminescence signal. Continuous-wave excitation using the 520-nm laser corresponds to 11.5 mW of optical power. The resulting photoluminescence is measured as roughly 12 Mcps, with a 0.11% signal fluctuation. The average optical power delivered to the sample is much lower for pulsed measurements such as ODMR, Rabi oscillations, and Hahn echos, resulting in significantly lower average photoluminescence count rates.

Both the B_0 magnetic field from the superconducting solenoid and the B_1 mode from the dielectric resonator are oriented along the z axis, corresponding to the [100] crystal direction. This leads to quenching of the photoluminescence of the $N-V^-$ centers at relatively low B_0 intensities, as the quantization axes shift away from the $\langle 111 \rangle N-V^-$ axes [59]. A related issue is that the dielectric resonator frequency must be tuned to the ODMR frequency of the $N-V^-$ centers for meaningful measurements. A high 520-nm laser power could heat the dielectric resonator to such an extent that the B_0 field must be increased accordingly to shift the ODMR frequency closer to the resonator frequency. A trade-off between the laser power and the magnetic field quenching must be made so as to optimize the signal-to-noise ratio for spin-signal measurements. Therefore, a magnetic field of roughly 5 mT is used for the spin measurements, which allows

for sufficient spin-signal detection without significant quenching.

A summary of the instruments used and their applications is given in Table I.

2. CST magnetic field simulation

The coupling between the loop coupler and the sample stack is simulated in CST MICROWAVE STUDIO. The simulation results are plotted in Fig. 9. The relevant simulation parameters are given in Table II. The simulation parameters are adjusted to match the experimental setup conditions and the measured coupling.

The mode volume of the dielectric resonator is calculated from the simulated H field (in amperes per meter) of the structure. The relevant expression is given as $V_m = \int_V (|H^2(r)| / |H_{\max}^2(r)|) dV$ [28]. The integral is evaluated over the H field generated by the structure and $H_{\max}(r)$ represents the maximum H -field intensity found within the structure.

3. Quality-factor comparison

We observe that the quality factor of the coupled dielectric resonator is generally much lower than expected. Upon further investigation, we determine that it is in fact the

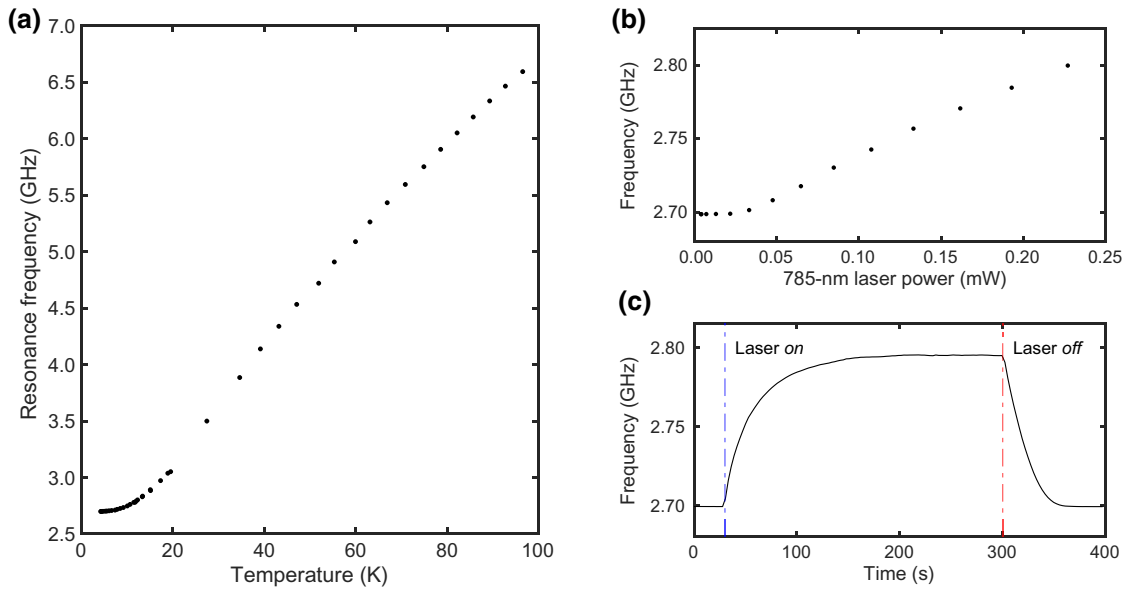


FIG. 7. The dielectric resonator-frequency tuning. (a) The dielectric resonator frequency measured as a function of the cryostat temperature. (b) The dielectric resonator frequency as a function of the infrared laser power as measured at the optical window into the cryostat. (c) The temporal step response of the dielectric resonator frequency after infrared laser modulation.

$N-V^-$ diamond sample that is responsible for the low quality factors. A simple test of conductivity along the edges of the sample shows a sheet resistance of approximately $240\ \Omega$, strongly suggesting the presence of a conductive graphite layer that may have originated from laser cutting.

We have also tested a different electronic grade diamond sample that has been appropriately cleaned, showing no measurable conductivity. We use this electronic grade diamond sample as a reference sample to test for high quality factors together with the dielectric resonator.

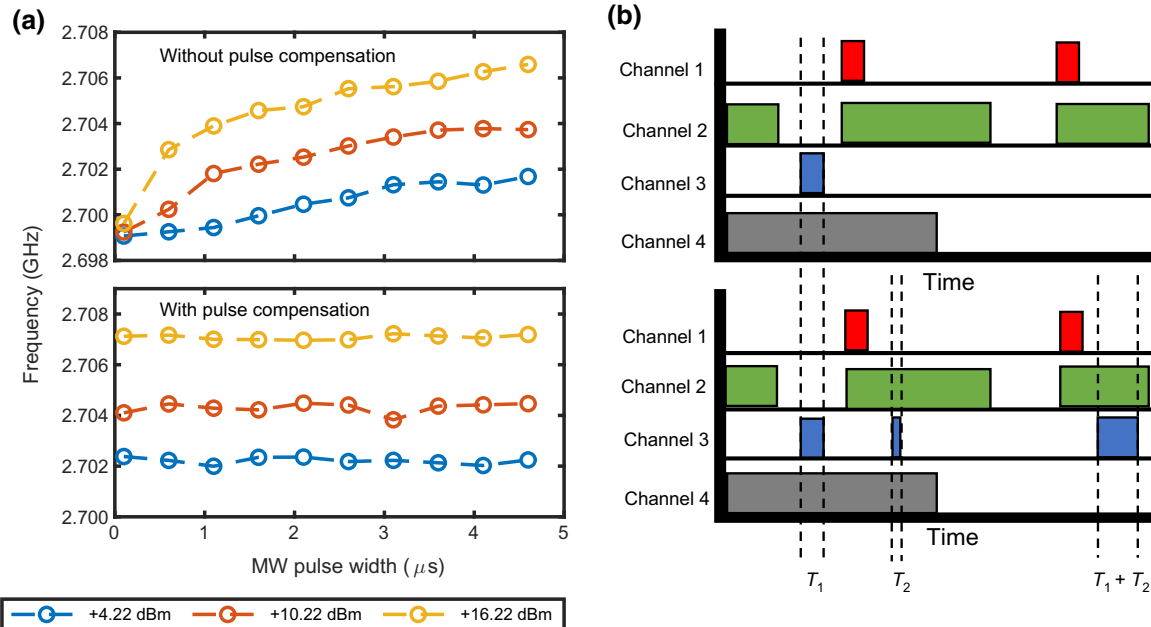


FIG. 8. The dielectric resonator-frequency stabilization. (a) The resonator-frequency drift is likely due to heating caused by longer microwave pulses and higher microwave powers when no pulse compensation is employed. All lasers are off. (b) The resonator frequency is stabilized by keeping the total microwave duty cycle ($T_1 + T_2$) constant for various microwave pulse widths (T_1). In the first half cycle, a measurable ODMR signal is created, while the second half cycle acts as reference for the lock-in amplifier: channel 1, detector gating; channel 2, 520-nm laser excitation; channel 3, microwave pulse; channel 4, lock-in reference.

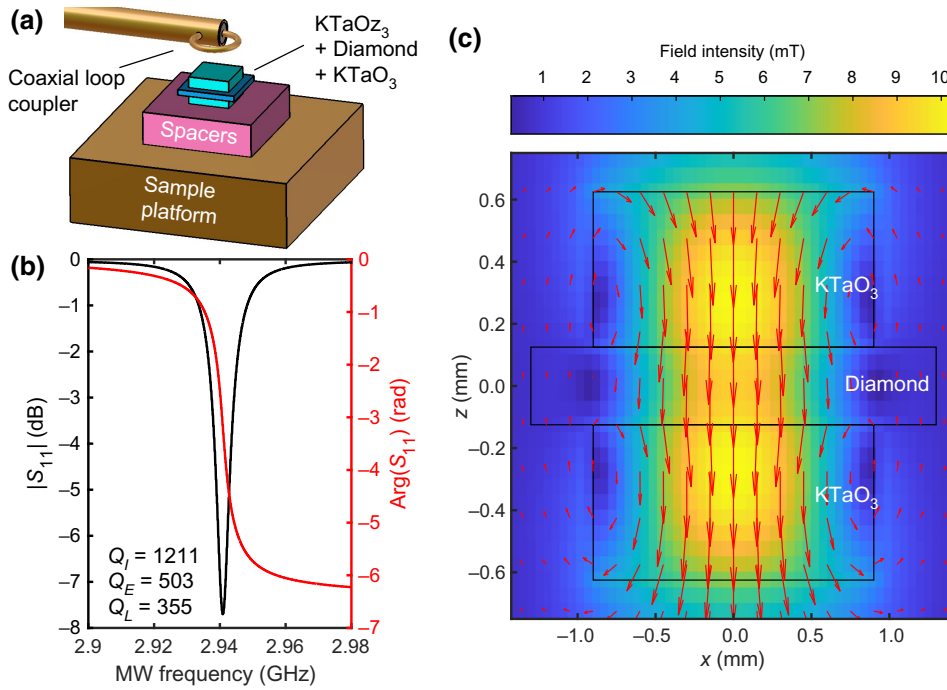


FIG. 9. The magnetic field simulation. (a) The simulation model, showing the loop coupler and relevant samples stacked on a conductive platform. (b) The simulated S_{11} magnitude, showing fitted quality factors similar to measured values in Fig. 1(c). (c) The simulated magnetic field distribution within the relevant sample volume with 1 W of applied microwave power at the loop coupler.

We also conduct quality-factor measurements of various diamond sample and dielectric resonator combinations, using an appropriate enclosure in liquid helium. The results of these quality-factor measurements are summarized in Table III. By matching the simulated and measured quality factors, we estimate the loss tangent of the electronic grade diamond sample to be approximately 10^{-4} , which is roughly comparable to the literature values for the relevant temperature and frequency range [60,61]. Similarly, the

loss tangent of the $N-V^-$ diamond sample is also estimated to be 1.25 by matching the measured and simulated quality factors and is found to be 4 orders of magnitude higher than expected. This high loss tangent for the $N-V^-$ diamond sample is consistent with our surface-conductivity measurements of the sample, attributed to the graphite layer.

4. B_1 conversion factor

To calculate a fair estimate for the microwave power-to- B_1 conversion factor C_P , we take into account the four possible orientations of the $N-V^-$ axes, the microwave line loss, and the insertion loss of the various microwave components used, as well as the power reflected from the coaxial

TABLE I. A list of all the relevant instruments and/or apparatus used.

| Instrument | Application |
|---------------------------------------|--|
| Bluefors LD Dilution refrigerator;IMG | Cryostat (4 K using only pulse tube cooling) |
| Keysight N5183B MXG | Microwave source |
| Agilent 8753ES | Vector network analyzer |
| CentricRF CF2040 | Microwave circulator |
| Spincore PulseBlasterESR-PRO | Pulse generator |
| Minicircuits ZACS622 -100WSX+ | Microwave power combiner |
| Minicircuits ZHL-5W-63-S+ | Microwave power amplifier |
| SRS SR830 | Lock-in amplifier |
| Attocube ANSxy100lr + ANSz100std | Piezoelectric positioner |
| Excelitas SPCM-ARQH-10-FC | Single-photon detector |
| Thorlabs LP520-SF15 | 520-nm laser diode |
| Thorlabs FPL785P-200 + CLD1015 | 785-nm laser diode + laser driver |

TABLE II. A summary of the relevant parameters used in the CST simulation model.

| Parameter | Value | Description |
|-------------------|----------------------|---|
| d1 | 1 mm | Coax inner-conductor diameter |
| d2 | 1.25 mm | Separation between top KTaO ₃ resonator and loop coupler |
| ϵ_{rk} | 3300 | KTaO ₃ relative permittivity |
| ϵ_{rd} | 5.68 | Diamond relative permittivity |
| ϵ_{rs} | 9.4 | Sapphire relative permittivity |
| Tan δ_k | 2.5×10^{-5} | KTaO ₃ dielectric loss tangent |
| Tan δ_{d1} | 1.25 | $N-V^-$ diamond dielectric loss tangent |
| Tan δ_{d2} | 10^{-4} | Electronic grade diamond dielectric loss tangent |
| Tan δ_s | 4×10^{-4} | Sapphire dielectric loss tangent |
| ρ_c | 2×10^8 | platform conductivity |

TABLE III. A comparison of the quality (Q) factors of various samples and arrangements. Q_I , Q_L , and Q_E refer to internal, loaded, and external coupling, respectively.

| Single KTaO₃ | |
|--|-----------------------|
| Q_I | $61\,240 \pm 330$ |
| Q_L | $31\,220 \pm 110$ |
| Q_E | $63\,690 \pm 150$ |
| Single KTaO₃ + N-V⁻ CVD diamond | |
| Q_I | $3\,360 \pm 80$ |
| Q_L | $2\,990 \pm 70$ |
| Q_E | $27\,840 \pm 460$ |
| KTaO₃ sandwich + N-V⁻ CVD diamond | |
| Q_I | $2\,340 \pm 50$ |
| Q_L | $2\,060 \pm 40$ |
| Q_E | $17\,050 \pm 250$ |
| Single KTaO₃ + electronic grade CVD diamond | |
| Q_I | $57\,400 \pm 1\,000$ |
| Q_L | $46\,400 \pm 800$ |
| Q_E | $243\,000 \pm 3\,000$ |

loop coupler. Our microwave losses, including insertion losses and reflection, as well as the amplifier gain, are quantified in Table IV.

There is some microwave power that is reflected from the loop coupler. We can compensate for this reflected power from the loop coupler by measuring the S_{11} (dB) parameter using the VNA. The appropriate “gain” G_c in dB is given by

$$G_c = 10 \log_{10} (1 - (10^{\frac{S_{11}}{20}})^2) \quad (\text{A1})$$

and represents the transmission loss. This value is simply added to the microwave line gains and losses shown in Table IV (excluding the reflection loss). This value can also be used to compensate the measured Rabi frequencies,

TABLE IV. A list of all the relevant microwave losses and gains in the microwave line.

| Component | Gain or loss (dB) | Description |
|---|-------------------|-------------------------------------|
| Room-temperature cables and attenuators | -33.06 | Attenuators and cable loss |
| MW power amplifier | +45.41 | Amplifier gain |
| MW power combiner | -3.36 | Insertion loss |
| Cryostat MW line | -3.34 | 2.967 GHz, 4 K |
| MW circulator | -0.60 | Insertion loss |
| Reflection loss | -0.83 | $S_{11} = -7.60$ dB, using Eq. (A1) |
| Total | +4.22 | |

TABLE V. A description of the parameters used in the laser-intensity function.

| Parameter | Value | Description |
|-------------|-------------------|--------------------------|
| D | 2.2 mm | Collimated beam diameter |
| λ | 520 nm | Laser wavelength |
| f_l | 15.29 mm | Lens focal length |
| M | 1 | Beam ellipticity |
| $2W_0$ | 4.6 μm | Focused spot diameter |
| $\mu_{x,y}$ | 0 mm | Beam displacement |

due to changes in reflection loss as a result of changed coupling positions of the dielectric resonator to the loop coupler.

The B_1 field is known to be strongly oriented in the [100] direction. An approximation can be made that all four N-V⁻ orientations thus experience the B_1 field at the same angle, corresponding to roughly $\alpha = 54.7^\circ$. The measured Rabi frequency is given by the relationship $\Omega_R = (1/\sqrt{2})\gamma_e B_{1\perp}$, where $B_{1\perp}$ is the perpendicular (to the N-V⁻) component of the total B_1 field driving the spins. The total B_1 magnitude is thus given as $B_1 = (B_{1\perp}/\sin \alpha)$ [14].

5. Rabi coherence simulation

Simulation of the Rabi oscillation decay times requires the following parameters:

- (a) The static magnetic field vector B_0 .
- (b) The simulated ac magnetic field (B_1) vectors and frequency.
- (c) The Gaussian ensemble broadening.
- (d) The hyperfine coupling (MHz).
- (e) The laser intensity within the sample volume.

The B_0 field vector and the ensemble-broadening parameters allow us to calculate the Rabi-oscillation signal contributions arising from detuned spin transitions. The OMDR transition frequencies themselves can be calculated from solving the relevant eigenvalues of the N-V⁻ Hamiltonian, similar to Ref. [46]. Though Rabi oscillations can be calculated directly from the Hamiltonian as well, it is preferable

TABLE VI. The optimized simulation parameters for the simulation shown in Fig. 2(a) in the main text. All angles are given with respect to the [100] crystallographic direction.

| Parameter | Value |
|------------------------------|-------------------------------|
| Ensemble broadening | 1.868 ± 0.054 MHz |
| B_1 angle | $3.723^\circ \pm 0.012^\circ$ |
| B_0 angle | 0.000° |
| B_0 magnitude | 5.031 ± 0.023 mT |
| D_z (zero field splitting) | 2.878 GHz |
| Hyperfine | 2.15 MHz |

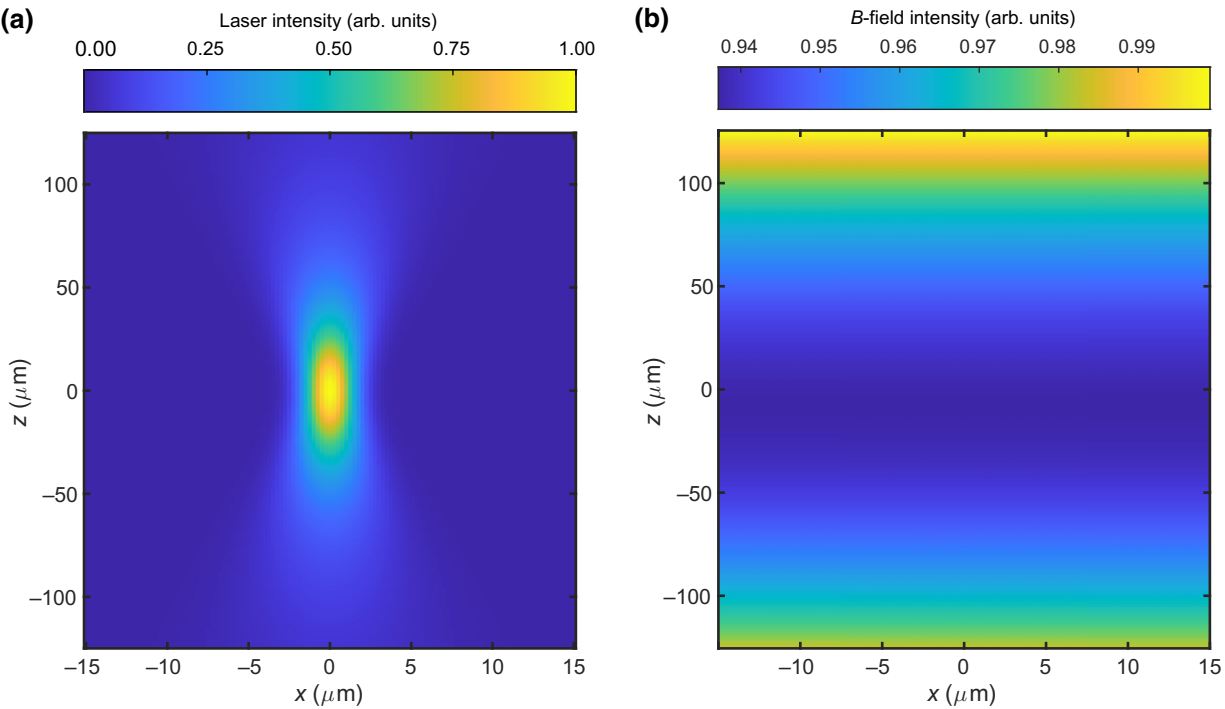


FIG. 10. Laser excitation and magnetic field simulations. (a) A cross-section plot of the 520-nm laser-intensity model within the signal collection volume, showing a minimum beam waist of $4.6 \mu\text{m}$ at the focus. (b) A plot of the simulated B -field magnitude within the signal collection volume: the B -field intensity is rescaled.

to use the analytical Rabi formula in the rotating frame given in Eq. (A2) to reduce the computation time:

$$P_{N|\uparrow} = \frac{\omega_{1,N}^2}{\Delta\omega^2 + \omega_{1,N}^2} \sin^2 \left(\frac{\sqrt{\Delta\omega^2 + \omega_{1,N}^2}}{2} t \right). \quad (\text{A2})$$

The B_1 field within the signal collection volume is obtained from a finite element method (FEM) simulation of the structure, and is plotted in Fig. 10(b). The B_1 field is expressed in the Rabi formula Eq. (A2) as a Rabi frequency $\omega_{1,N}(x,y,z)$ that is calculated for each $N-V^-$ orientation labelled by the subscript N and for each coordinate (x,y,z) within the volume of interest. The B_1 data is scaled for each power level according to the conversion factor C_p , as measured in Fig 2(b). Further, as we know that the component of the B_1 field perpendicular to the $N-V^-$ axis is responsible for the oscillations, we must scale the B_1 field by a factor of $(\sin(\theta)/\sin(54.7^\circ))\Omega_R$ (approximation). Here, θ represents the angle (in degrees) between the $N-V^-$ axes and the magnetic field vector B_1 .

The signal collection volume is effectively given by a simple Gaussian laser-intensity function within the diamond sample volume:

$$f(x,y,z) = \left(\frac{W_0}{w_z} \right)^2 e^{-2\left(\frac{x-\mu_x}{w_z}\right)^2} e^{-2\left(\frac{y-\mu_y}{w_z}\right)^2} \quad (\text{A3})$$

$$W_0 = \frac{4M^2\lambda f_l}{2\pi D}, \quad (\text{A4})$$

$$w_z = W_0 \sqrt{1 + \left(\frac{z\lambda}{\pi W_0^2} \right)^2}. \quad (\text{A5})$$

The parameters of this function are summarized in Table V.

The excitation laser spot size is calculated to be $4.6 \mu\text{m}$, given the lens focal length of 15.29 mm and a collimated beam diameter of 2.2 mm. Then, using Eqs. (A2) and (A3), we derive the total Rabi signal as a function of time and summed over the $N = 4$ possible $N-V^-$ orientations as given in Eq. (A6):

$$\Omega_R(t) = \sum_{N=1}^4 \int_V f(x,y,z) P_{N|\uparrow}(\omega_1(x,y,z), t) dV. \quad (\text{A6})$$

The limits of the integration represent the bounds of the sample volume of interest as illuminated by the laser. It is the decay time constant of this signal that corresponds to the T_2^{Rabi} coherence time.

The nonlinear data fitting is accomplished using the MATLAB global-optimization toolbox. Rough fitting is

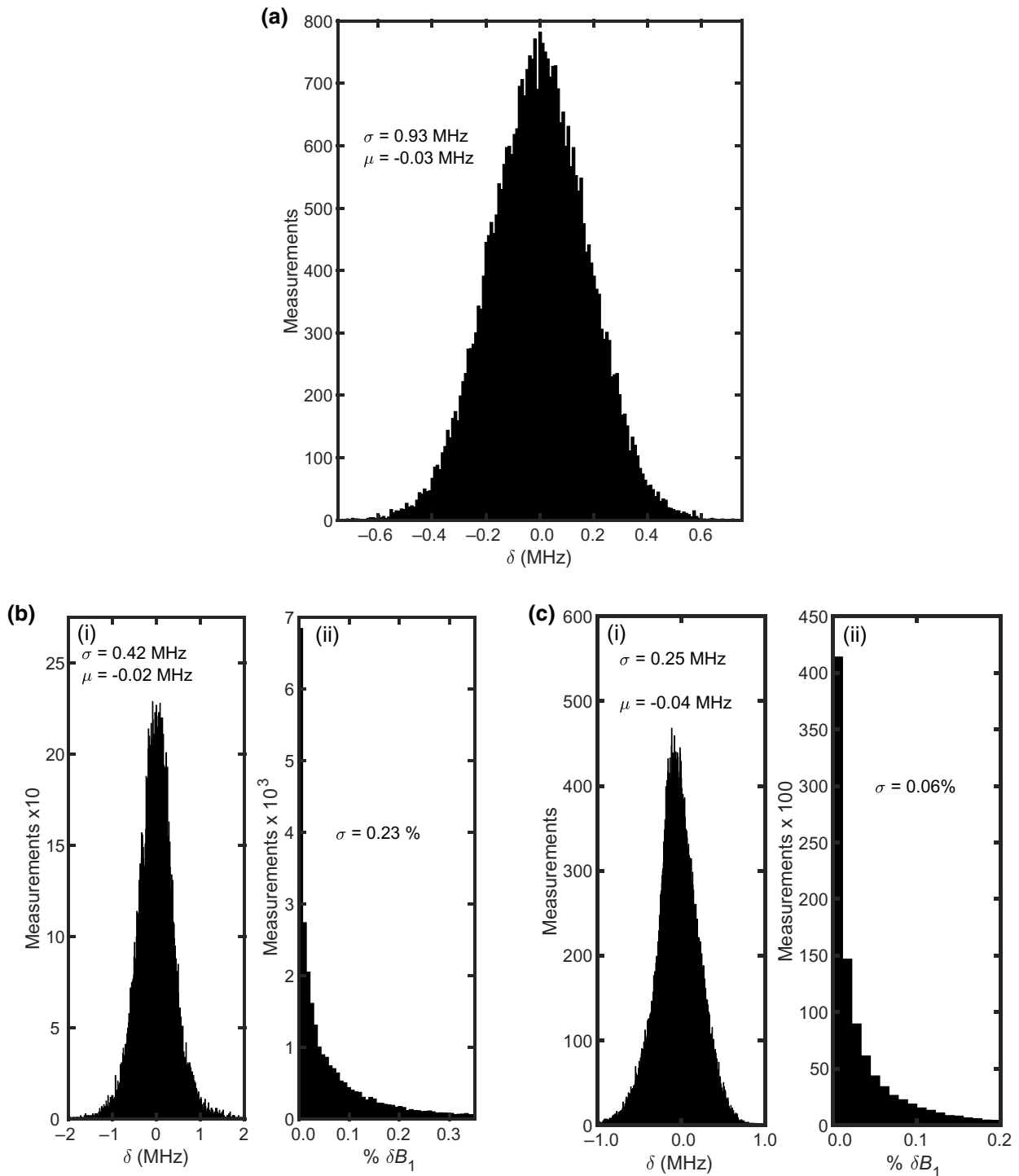


FIG. 11. The dielectric resonator-frequency stability. (a) The resonator deviation from 2.967 GHz as recorded while implementing continuous resonator tuning during the ODMR measurement shown in Fig. 1(d) in the main text. (b) The histogram of the resonator-frequency deviation from the set point, accumulated throughout the measurement corresponding to Fig. 2 in the main text. The corresponding histogram data shows the distribution in terms of percentage change of the Rabi frequencies (δB_1) as a result of resonator deviation. The calculation of δB_1 uses measured data shown in Fig. 3 in the main text. (c) The combined histogram of all measured resonator deviation values from the detuning set points used for the measurement shown in Fig. 3 in the main text.

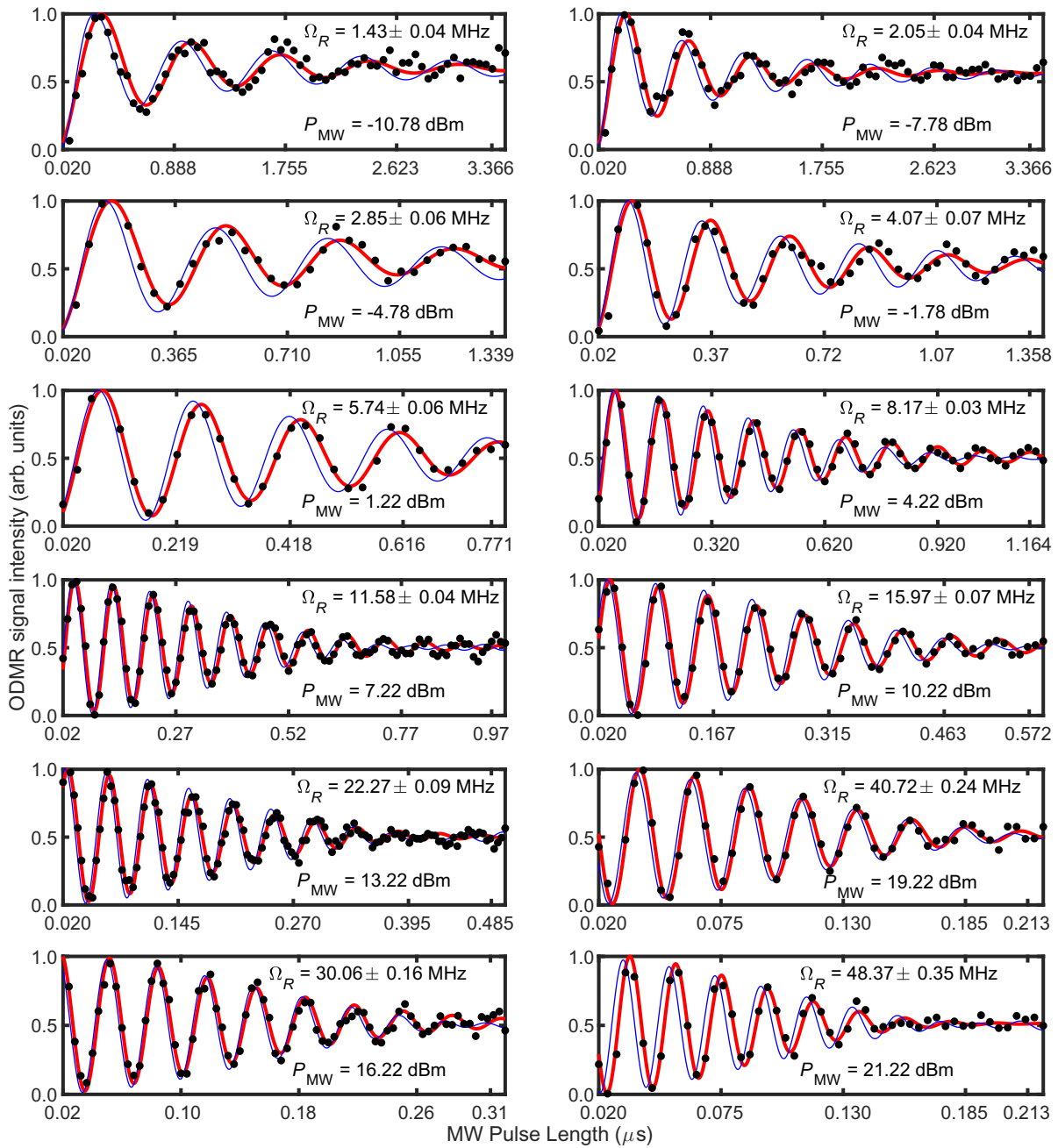


FIG. 12. The collection of the measured (red) and simulated (blue) Rabi signals for assorted applied microwave powers. The measured data are fitted to the function $f(t) = e^{-(t/\tau)^n} \sin(2\pi\Omega_R t + p) + c$.

done with the “PatternSearch” algorithm and finer fits are accomplished by the “NLINFIT” function, which can also provide fit-parameter confidence intervals. The list of fit parameters and their values is given in Table VI.

In our simulations, we find that we require approximately 3.7° of tilt in the B_1 vector for the simulation results to match the measurement data. We partly attribute this tilt to imprecise sample mounting and a crystallographic

mis cut of the diamond sample. The manufacturer’s specification of the crystallographic orientation miscut tolerance is given as $\pm 3^\circ$ [56].

While there is some instability in the resonator frequency, despite our control and/or tuning mechanism (see Fig. 11), we find that such instability does not significantly impact the coherence times of our Rabi oscillations.

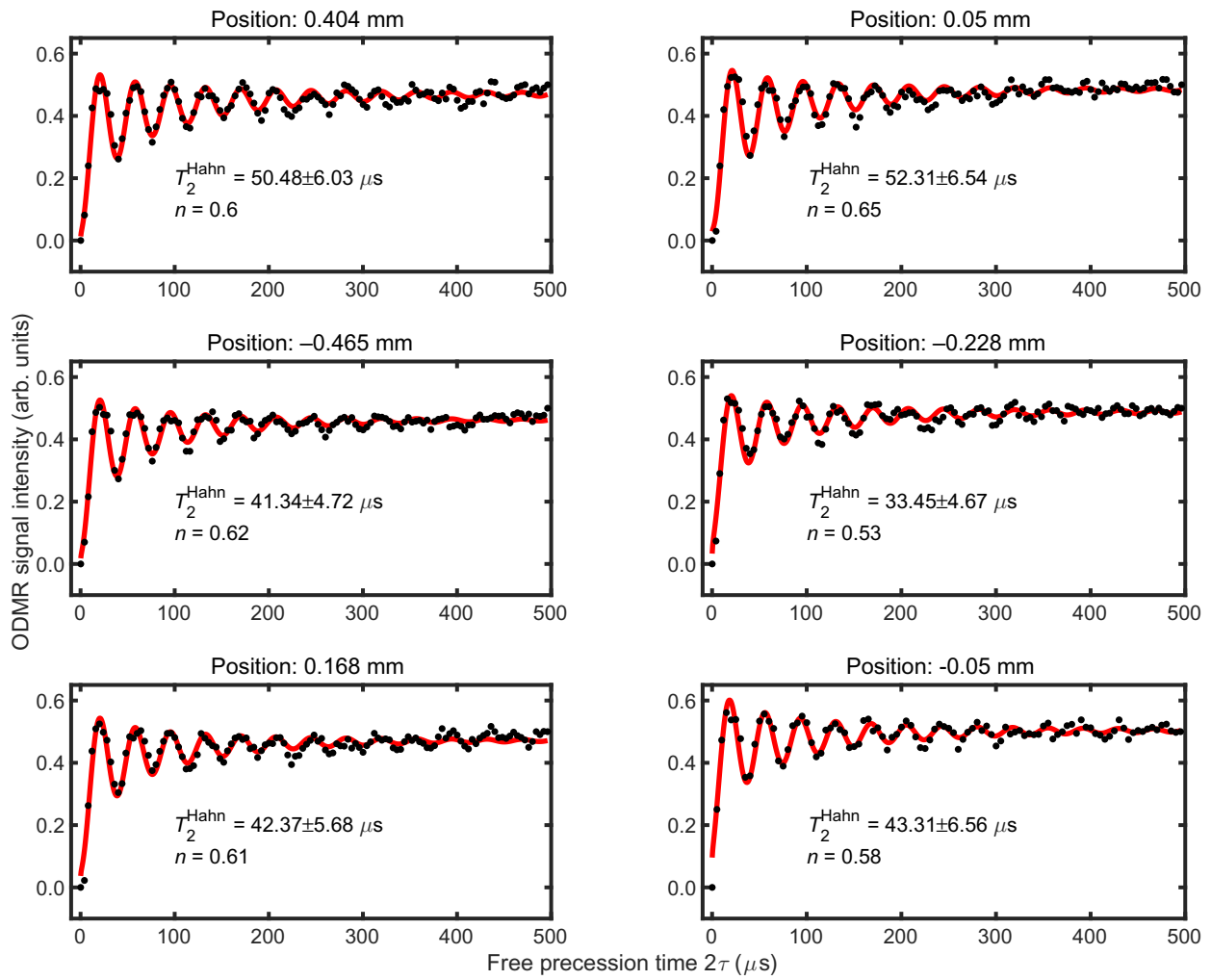


FIG. 13. The collection of the measured and fitted τ^2 Hahn-echo signals for various positions along the x axis of the resonator. The data points at the end of the measured signals are scaled to 0.5 to represent the spins entering into a mixed state. The fit function used is $f(t) = e^{-(t/\tau)^n}(a_1 + a_2(\sin^2(0.5\omega t + p))) + c$.

-
- [1] D. P. DiVincenzo, The physical implementation of quantum computation, *Fortschr. Phys.* **48**, 771 (2000).
 - [2] M. A. Nielsen and I. Chuang, Quantum computation and quantum information (2002).
 - [3] W. Yang, Z.-Y. Wang, and R.-B. Liu, Preserving qubit coherence by dynamical decoupling, *Front. Phys. China* **6**, 2 (2011).
 - [4] D. A. Lidar and T. A. Brun, *Quantum Error Correction* (Cambridge University Press, Cambridge, 2013).
 - [5] J. M. Le Floch, C. Bradac, N. Nand, S. Castelletto, M. E. Tobar, and T. Volz, Addressing a single spin in diamond with a macroscopic dielectric microwave cavity, *Appl. Phys. Lett.* **105**, 133101 (2014).
 - [6] E. Vahapoglu, J. P. Slack-Smith, R. C. C. Leon, W. H. Lim, F. E. Hudson, T. Day, T. Tanttu, C. H. Yang, A. Laucht, A. S. Dzurak, and J. J. Pla, Single-electron spin resonance

in a nanoelectronic device using a global field, *Sci. Adv.* **7** (2021).

- [7] J. Ebel, T. Joas, M. Schalk, P. Weinbrenner, A. Angerer, J. Majer, and F. Reinhard, Dispersive readout of room-temperature spin qubits, *Quantum Sci. Technol.* **6**, 03LT01 (2021).
- [8] E. R. Eisenach, J. F. Barry, M. F. O'Keeffe, J. M. Schloss, M. H. Steinecker, D. R. Englund, and D. A. Braje, Cavity-enhanced microwave readout of a solid-state spin sensor, *Nat. Commun.* **12**, 1 (2021).
- [9] M. Chipaux, A. Tallaire, J. Achard, S. Pezzagna, J. Meijer, V. Jacques, J. F. Roch, and T. Debuisschert, Magnetic imaging with an ensemble of nitrogen vacancy-centers in diamond, *Eur. Phys. J. D* **69**, 166 (2015).
- [10] K. Bayat, J. Choy, M. Farrokh Baroughi, S. Meesala, and M. Loncar, Efficient, uniform, and large area microwave magnetic coupling to NV centers in diamond using double split-ring resonators, *Nano Lett.* **14**, 1208 (2014).

- [11] K. Sasaki, Y. Monnai, S. Saito, R. Fujita, H. Watanabe, J. Ishi-Hayase, K. M. Itoh, and E. Abe, Broadband, large-area microwave antenna for optically detected magnetic resonance of nitrogen-vacancy centers in diamond, *Rev. Sci. Instrum.* **87**, 053904 (2016).
- [12] J. Herrmann, M. A. Appleton, K. Sasaki, Y. Monnai, T. Teraji, K. M. Itoh, and E. Abe, Polarization- and frequency-tunable microwave circuit for selective excitation of nitrogen-vacancy spins in diamond, *Appl. Phys. Lett.* **109**, 183111 (2016).
- [13] M. Mrózek, J. Mlynarczyk, D. S. Rudnicki, and W. Gawlik, Circularly polarized microwaves for magnetic resonance study in the GHz range: Application to nitrogen-vacancy in diamonds, *Appl. Phys. Lett.* **107**, 013505 (2015).
- [14] E. R. Eisenach, J. F. Barry, L. M. Pham, R. G. Rojas, D. R. Englund, and D. A. Braje, Broadband loop gap resonator for nitrogen vacancy centers in diamond, *Rev. Sci. Instrum.* **89**, 94705 (2018).
- [15] R. R. Mett, J. W. Sidabras, J. R. Anderson, C. S. Klug, and J. S. Hyde, Rutile dielectric loop-gap resonator for X-band EPR spectroscopy of small aqueous samples, *J. Mag. Res.* **307**, 106585 (2019).
- [16] V. Yaroshenko, V. Soshenko, V. Vorobyov, S. Bolshedovskii, E. Nenasheva, I. Kotel'nikov, A. Akimov, and P. Kapitanova, Circularly polarized microwave antenna for nitrogen vacancy centers in diamond, *Rev. Sci. Instrum.* **91**, 035003 (2020).
- [17] Y. Wang, Y. Liu, H. Guo, X. Han, A. Cai, S. Li, P. Zhao, and J. Liu, Integrated microwave cavity and antenna to improve the sensitivity of diamond NV center spin-based sensors, *Appl. Phys. Express* **13**, 112002 (2020).
- [18] P. Andrich, C. F. de las Casas, X. Liu, H. L. Bretscher, J. R. Berman, F. J. Heremans, P. F. Nealey, and D. D. Awschalom, Long-range spin wave mediated control of defect qubits in nanodiamonds, *Npj Quantum Inf.* **3**, 28 (2017).
- [19] J. P. Dehollain, J. J. Pla, E. Siew, K. Y. Tan, A. S. Dzurak, and A. Morello, Nanoscale broadband transmission lines for spin qubit control, *Nanotechnology* **24**, 15202 (2013).
- [20] A. Bienfait, J. J. Pla, Y. Kubo, M. Stern, X. Zhou, C. C. Lo, C. D. Weis, T. Schenkel, M. L. Thewalt, D. Vion, D. Esteve, B. Julsgaard, K. Mølmer, J. J. Morton, and P. Bertet, Reaching the quantum limit of sensitivity in electron spin resonance, *Nat. Nanotech.* **11**, 253 (2015).
- [21] G. D. Fuchs, V. V. Dobrovitski, D. M. Toyli, F. J. Heremans, and D. D. Awschalom, Gigahertz dynamics of a strongly driven single quantum spin, *Science* **326**, 1520 (2009).
- [22] J. W. Sidabras, J. Duan, M. Winkler, T. Happe, R. Hussein, A. Zouni, D. Suter, A. Schnegg, W. Lubitz, and E. J. Reiherse, Extending electron paramagnetic resonance to nanoliter volume protein single crystals using a self-resonant microhelix, *Sci. Adv.* **5** (2019).
- [23] G. Annino, M. Cassettari, I. Longo, and M. Martinelli, Dielectric resonators in ESR: Overview, comments and perspectives, *App. Mag. Res.* **16**, 45 (1999).
- [24] W. M. Walsh and L. W. Rupp, Enhanced ESR sensitivity using a dielectric resonator, *Rev. Sci. Instrum.* **57**, 2278 (1986).
- [25] I. N. Geifman and I. S. Golovina, Application of ferroelectrics in radiospectroscopy, *Ferroelectrics* **333**, 89 (2006).
- [26] E. Abe, H. Wu, A. Ardavan, and J. J. Morton, Electron spin ensemble strongly coupled to a three-dimensional microwave cavity, *Appl. Phys. Lett.* **98**, 251108 (2011).
- [27] J.-M. Le Floch, N. Delhote, M. Aubourg, V. Madrangeas, D. Cros, S. Castelletto, and M. E. Tobar, Towards achieving strong coupling in three-dimensional-cavity with solid state spin resonance, *J. Appl. Phys* **119**, 153901 (2016).
- [28] J. D. Breeze, E. Salvadori, J. Sathian, N. M. N. Alford, and C. W. Kay, Continuous-wave room-temperature diamond maser, *Nature* **555**, 493 (2018).
- [29] R. G. Geyer, B. Riddle, J. Krupka, and L. A. Boatner, Microwave dielectric properties of single-crystal quantum paraelectrics KTaO_3 and SrTiO_3 at cryogenic temperatures, *J. Appl. Phys.* **97**, 104111 (2005).
- [30] E. S. Sabisky and H. J. Gerritsen, Measurements of dielectric constant of rutile (TiO_2) at microwave frequencies between 4.2 and 300 K, *J. Appl. Phys.* **33**, 1450 (1962).
- [31] J. Krupka, K. Derzakowski, M. Tobar, J. Hartnett, and R. G. Geyer, Complex permittivity of some ultra low loss dielectric crystals at cryogenic temperatures, *Meas. Sci. Technol.* **10**, 387 (1999).
- [32] M. Shinoda, K. Saito, and T. Kondo, High-density near-field readout using solid immersion lens made of KTaO_3 monocrystal, *Jpn. J. Appl. Phys.* **45**, 1332 (2006).
- [33] K. Fujiura and M. Sasaura, KTaO_3 solid immersion lens for nearfield optical disk system, *NTT Tech. Rev.* **5** (2007).
- [34] I. N. Geifman, I. S. Golovina, E. R. Zusmanov, and V. I. Kofman, Raising the sensitivity of the electron-paramagnetic-resonance spectrometer using a ferroelectric resonator, *Tech. Phys.* **45**, 263 (2000).
- [35] A. Blank, E. Stavitski, H. Levanon, and F. Gubaydullin, Transparent miniature dielectric resonator for electron paramagnetic resonance experiments, *Rev. Sci. Instrum.* **74**, 2853 (2003).
- [36] M. W. Doherty, N. B. Manson, P. Delaney, F. Jelezko, J. Wrachtrup, and L. C. Hollenberg, The nitrogen-vacancy colour centre in diamond, *Phys. Rep.* **528**, 1 (2013), the nitrogen-vacancy colour centre in diamond.
- [37] L. Rondin, J.-P. Tetienne, T. Hingant, J.-F. Roch, P. Maletinsky, and V. Jacques, Magnetometry with nitrogen-vacancy defects in diamond, *Rep. Prog. Phys.* **77**, 056503 (2014).
- [38] P. Appel, M. Ganzhorn, E. Neu, and P. Maletinsky, Nanoscale microwave imaging with a single electron spin in diamond, *N. J. Phys* **17**, 112001 (2015).
- [39] A. Horsley, P. Appel, J. Wolters, J. Achard, A. Tallaire, P. Maletinsky, and P. Treutlein, Microwave Device Characterization Using a Widefield Diamond Microscope, *Phys. Rev. Appl.* **10**, 044039 (2018).
- [40] B. Yang, M. M. Dong, W. H. He, Y. Liu, C. M. Feng, Y. J. Wang, and G. X. Du, Using diamond quantum magnetometer to characterize near-field distribution of patch antenna, *IEEE Trans. Microwave Theory Tech.* **67**, 2451 (2019).
- [41] K. Nemoto, M. Trupke, S. J. Devitt, B. Scharfenberger, K. Buczak, J. Schmiedmayer, and W. J. Munro, Photonic quantum networks formed from NV-centers, *Sci. Rep.* **6**, 1 (2016).

- [42] M. K. Bhaskar, R. Riedinger, B. Machielse, D. S. Levonian, C. T. Nguyen, E. N. Knall, H. Park, D. Englund, M. Lončar, D. D. Sukachev, and M. D. Lukin, Experimental demonstration of memory-enhanced quantum communication, *Nature* **580**, 60 (2020).
- [43] D. D. Sukachev, A. Sipahigil, C. T. Nguyen, M. K. Bhaskar, R. E. Evans, F. Jelezko, and M. D. Lukin, Silicon-Vacancy Spin Qubit in Diamond: A Quantum Memory Exceeding 10 ms with Single-Shot State Readout, *Phys. Rev. Lett.* **119**, 223602 (2017).
- [44] J. Wrachtrup and F. Jelezko, Processing quantum information in diamond, *J. Phys.: Cond. Matt.* **18**, 807 (2006).
- [45] H. Zhang, C. Belvin, W. Li, J. Wang, J. Wainwright, R. Berg, and J. Bridger, Little bits of diamond: Optically detected magnetic resonance of nitrogen-vacancy centers, *Am. J. Phys.* **86**, 225 (2018).
- [46] V. K. Sewani, H. H. Vallabhapurapu, Y. Yang, H. R. Firgau, C. Adambukulam, B. C. Johnson, J. J. Pla, and A. Laucht, Coherent control of NV-centers in diamond in a quantum teaching lab, *Am. J. Phys.* **88**, 1156 (2020).
- [47] C. P. Poole, *Electron Spin Resonance: a Comprehensive Treatise on Experimental Techniques* (Courier Corporation, 1996).
- [48] S. Probst, V. Ranjan, Q. Ansel, R. Heeres, B. Albanese, E. Albertinale, D. Vion, D. Esteve, S. J. Glaser, D. Sugny, and P. Bertet, Shaped pulses for transient compensation in quantum-limited electron spin resonance spectroscopy, *J. Mag. Res.* **303**, 42 (2019).
- [49] C. Adambukulam, V. K. Sewani, H. G. Stemp, S. Asaad, M. T. Madzik, A. Morello, and A. Laucht, An ultra-stable 1.5 T permanent magnet assembly for qubit experiments at cryogenic temperatures, *Rev. Sci. Instrum.* **92**, 085106 (2021).
- [50] L. Childress, M. V. Gurudev Dutt, J. M. Taylor, A. S. Zibrov, F. Jelezko, J. Wrachtrup, P. R. Hemmer, and M. D. Lukin, Coherent dynamics of coupled electron and nuclear spin qubits in diamond, *Science* **314**, 281 (2006).
- [51] P. L. Stanwix, L. M. Pham, J. R. Maze, D. Le Sage, T. K. Yeung, P. Cappellaro, P. R. Hemmer, A. Yacoby, M. D. Lukin, and R. L. Walsworth, Coherence of nitrogen-vacancy electronic spin ensembles in diamond, *Phys. Rev. B* **82**, 201201(R) (2010).
- [52] S. Takahashi, R. Hanson, J. van Tol, M. S. Sherwin, and D. D. Awschalom, Quenching Spin Decoherence in Diamond through Spin Bath Polarization, *Phys. Rev. Lett.* **101**, 047601 (2008).
- [53] E. Bauch, S. Singh, J. Lee, C. A. Hart, J. M. Schloss, M. J. Turner, J. F. Barry, L. M. Pham, N. Bar-Gill, S. F. Yelin, and R. L. Walsworth, Decoherence of ensembles of nitrogen-vacancy centers in diamond, *Phys. Rev. B* **102**, 134210 (2020).
- [54] N. Khaneja, Switched control of electron nuclear spin systems, *Phys. Rev. A* **76**, 032326 (2007).
- [55] S. S. Hegde, J. Zhang, and D. Suter, Efficient Quantum Gates for Individual Nuclear Spin Qubits by Indirect Control, *Phys. Rev. Lett.* **124**, 220501 (2020).
- [56] SC Plate CVD P2 diamond sample, Element 6, <https://e6cvd.com/us/application/all/sc-plate-cvd-2-6x2-6x0-25mm-100-p2.html> (2012).
- [57] M. D. Janezic and J. Baker-Jarvis, Full-wave analysis of a split-cylinder resonator for nondestructive permittivity measurements, *IEEE Trans. Microwave Theory Tech.* **47**, 2014 (1999).
- [58] C. Ang, A. S. Bhalla, and L. E. Cross, Dielectric behavior of paraelectric $KTaO_3$, $CaTiO_3$, and $(Ln_{1/2}Na_{1/2})TiO_3$ under a dc electric field, *Phys. Rev. B* **64**, 184104 (2001).
- [59] J. P. Tetienne, L. Rondin, P. Spinicelli, M. Chipaux, T. Debuisschert, J. F. Roch, and V. Jacques, Magnetic-field-dependent photodynamics of single NV defects in diamond: An application to qualitative all-optical magnetic imaging, *N. J. Phys* **14**, 103033 (2012).
- [60] V. Parshin, S. Myasnikova, V. Derkach, B. Garin, R. Heidinger, J. Molla, V. Ralchenko, S. Tarapov, I. Danilov, and V. Polyakov *et al.*, in *2005 Joint 30th International Conference on Infrared and Millimeter Waves and 13th International Conference on Terahertz Electronics* (IEEE, 2005), Vol. 1, p. 22.
- [61] J.-M. L. Floch, R. Bara, J. G. Hartnett, M. E. Tobar, D. Mouneyrac, D. Passerieux, D. Cros, J. Krupka, P. Goy, and S. Caroopen, Electromagnetic properties of polycrystalline diamond from 35 K to room temperature and microwave to terahertz frequencies, *J. Appl. Phys.* **109**, 094103 (2011).
- [62] S. Probst, F. B. Song, P. A. Bushev, A. V. Ustinov, and M. Weides, Efficient and robust analysis of complex scattering data under noise in microwave resonators, *Rev. Sci. Instrum.* **86**, 024706 (2015).